Title
Observed Wind and SST Variability off the California Coast During Summertime High Wind Events

Permalink
https://escholarship.org/uc/item/7wv8f8kj

Authors
Wu, Weiguang
Villas Boas, Ana Beatriz
Gille, Sarah T

Publication Date
2021-04-27

DOI
10.1002/essoar.10506894.1

Peer reviewed

The Seasonal Cycle of Significant Wave Height in the Ocean: Local vs Remote Forcing

Luke V. Colosi[1], Ana B. Villas Bôas[1], Sarah T. Gille[1]

[1]Scripps Institution of Oceanography, University of California San Diego, La Jolla, California

Key Points:

- Seasonal Wind Anomaly Regions occur in locations where the strongest winds do not coincide with the winter storm season.
- Local winds influence significant wave height within Seasonal Wind Anomaly Regions.
- Seasonal Wind Anomaly Regions in the Southern Hemisphere are less influenced by local winds than those in the Northern Hemisphere.

Corresponding author: Luke V. Colosi, `lcolosi@ucsd.edu`

Abstract

Significant wave height (SWH) stems from a combination of locally generated "wind-sea" and remotely generated "swell" waves. In the Northern and Southern Hemispheres, wave heights typically undergo a sinusoidal annual cycle, with larger SWH in winter in response to seasonal changes in high-latitude storm patterns that generate equatorward propagating swell. However, some locations deviate from this hemispheric-scale seasonal pattern in SWH. For example, in the California coastal region, local wind events occur in boreal spring and summer, leading to a wind speed (WSP) annual cycle with a distinct maximum in boreal spring and a corresponding local response in SWH. Here ocean regions with a WSP annual cycle reaching a maximum in late spring, summer, or early fall are designated as seasonal wind anomaly regions (SWARs). Intra-annual variability of surface gravity waves is analyzed globally using two decades of satellite-derived SWH and WSP data. The phasing of the WSP annual cycle is used as a metric to identify SWARs. Global maps of probability of swell based on wave age confirm that during the spring and summer months, locally forced waves are more statistically more likely in SWARs than in surrounding regions. The magnitude of the deviation in the SWH annual cycle is determined by the exposure to swell and characteristics of the wave field within the region. Local winds have a more identifiable impact on Northern Hemisphere SWARs than on Southern Hemisphere SWARs due to the larger seasonality of Northern Hemisphere winds.

Plain Language Summary

At the ocean surface, wave height can give insight into ocean-atmosphere interactions. Storms generate waves, which are known as swell when they propagate away from their point of origin. Swell waves account for most of the global ocean's surface waves. They vary annually, with large waves in the winter and small waves in the summer, due to seasonal changes in high-latitude storm systems. In some coastal areas, including the coast of California, local wind effects cause exceptionally high wind speeds in late spring. These strong local winds result in large waves in springtime, separate from the global-scale winter maximum in swell waves. Places with strong local winds during the late spring, summer, and early fall, here referred to as seasonal wind anomaly regions (SWARs), are identified using global satellite observations of wave height and wind speed. Details vary by location. SWAR wave fields depend on the exposure to swell as well as the strength

of the local winds. Compared with Southern Hemisphere storms, Northern Hemisphere storms have a stronger winter peak, which means that local winds have a larger influence in Northern Hemisphere SWARs than in Southern Hemisphere SWARs.

1 Introduction

Surface gravity waves are fundamental to ocean-atmosphere interactions, and they mediate exchanges of momentum, heat, gasses, and energy (Cavaleri et al., 2012; Edson et al., 2007; Sullivan et al., 2004; Villas Bôas et al., 2019). The flux of momentum from the wind to the wave field is the principal generation mechanism of surface waves (Ardhuin, 2020), which are commonly defined as having wave periods from 1 to 30 seconds (Munk, 1951). These waves can propagate long distances across the oceans away from their generation site (Snodgrass et al., 1966). The wave field in a particular location represents the superposition of locally forced waves, "wind-sea", and remotely forced waves, "swell" (Sverdrup & Munk, 1947; Semedo et al., 2011; Jiang & Chen, 2013; Villas Bôas et al., 2017).

Previous studies of the wave climate have focused on the global scale, for example by exploring the large-scale temporal trends and climate modes of the global wind and wave fields (e.g., I. R. Young, 1999; I. Young et al., 2011; Stopa & Cheung, 2014; Stopa, 2019; Echevarria et al., 2019) or by separating the wave field into swell and wind-sea components (e.g., Jiang & Chen, 2013; Semedo et al., 2011; Zheng et al., 2016). Although some regional analyses of the wave climate have been performed (Villas Bôas et al., 2017; Semedo, 2018; I. R. Young et al., 2020), there remains a gap in our understanding of how local atmospheric conditions influence the variability of the wave field.

Additionally, previous research, including studies by Semedo et al. (2011), Zheng et al. (2016), and Semedo (2018), has relied on wave model hindcasts to look at the characteristics of the global wave field for swell and wind-seas. In the present study, our goal is to provide an alternative observation-driven approach for exploring the influence of locally and remotely forced waves on the wave field at the global and regional scales.

Villas Bôas et al. (2017) showed that regional-scale wind variability can cause deviations in the seasonal cycle of significant wave height (SWH). They explored a distinct deviation occurring off the California coast due to a local wind phenomenon known as expansion fan winds, which are generated by a combination of atmospheric conditions

and coastal topography configuration (Winant et al., 1988). In the California Current region, expansion fan winds cause the wind speed (WSP) annual cycle to have a distinct maximum during late spring and early summer which lies outside the timing of the expected hemispheric-scale annual cycle. As a result, locally generated waves dominate the wave field up to 50% of the time during late spring and early summer, causing a seasonal augmentation in SWH relative to expected background SWH. Winant et al. (1988) hypothesized analogous wind events to be present in other oceanic regions that have coastal topography and atmospheric conditions similar to California and that may have similar wind speed annual cycle variability. These regions include the west coast of Australia, the coast of Namibia, the coast of Chile, the southern Caribbean sea, the northwest coast of Africa near Morocco, and the Arabian Sea near the tip of Somalia. This list includes eastern boundary current regions, monsoon regions, and regions significantly sheltered from remotely forced waves. Here, we refer to ocean regions that have a WSP annual cycle reaching a maximum during the late spring, summer, or early fall collectively as Seasonal Wind Anomaly Regions (SWARs). To our knowledge, there has been no exploration of the possible influence of regional-scale wind variability on the intra-annual variability of SWH in SWARs.

In this study, we identify SWARs globally and assess whether the seasonality seen in the California Current region is typical of other SWARs, characterized by local effects that are out of sync with high-latitude winter storms. Global-scale satellite observations of SWH and WSP from 1993 to 2015 are used to identify the WSP seasonal cycle, and SWARs are identified based on the timing of this cycle relative to the expected hemispheric-scale annual cycle of WSP. Implications for wave climate are then assessed from the relative timing of the WSP and SWH seasonal cycles. The work presented here contributes to the current understanding of the wave climate in regions that are partially dominated by wind-seas, which may have relevance for sea-state dependent air-sea fluxes (Villas Bôas et al., 2019), management of coastal resources, as well as shipping and navigation (Stopa, 2019; Ardhuin et al., 2019).

This paper is organized as follows: Section 2 describes the data sets and methods used to analyze global SWH and WSP. Section 3 explores the parameters of the annual and semi-annual SWH and WSP least-squares models globally and regional climatologies of potential expansion fan wind SWARs. This section also examines whether SWH

measurements during the late spring, summer or early fall months within SWARs are caused by locally or remotely generated waves. Section 4 summarizes our conclusions.

2 Data and Methods

2.1 Remotely Sensed Data

Wave data used in this study are drawn from over two decades (1 January 1993 to 31 December 2015) of cross-calibrated satellite altimeter SWH measurements produced by the Institut français de recherche pour l'exploitation de la mer (IFREMER) (Queffeulou & Croizé-Fillon, 2017; Queffeulou, 2004). IFREMER's SWH altimeter data set ensures near homogeneity of SWH measurements between multiple near-pole non-sun-synchronous satellites, which are calibrated against buoy observations. Here, we binned the daily along-track data onto a 1° by 1° spatial grid. Satellites incorporated in this IFREMER product include ERS-1&2, TOPEX-Poseidon, GEOSAT Follow-ON, Jason-1, Jason-2, EN-VISAT, Cryosat and SARAL AltiKa (see Queffeulou & Croizé-Fillon, 2017; Queffeulou, 2004).

Sea surface wind data were obtained from the Cross Calibrated Multi-Platform version 2 (CCMP2) wind vector analysis produced by Remote Sensing Systems (Atlas et al., 2011). CCMP2's data product is released on a 0.25° by 0.25° spatial grid with 6 hourly temporal resolution. For this analysis, we averaged CCMP2 winds spatially to a 1° by 1° grid and temporally to daily resolution in order to match the gridded SWH data. The CCMP2 product incorporates measurements from scatterometers, radiometers, in situ buoys, and modelled wind velocity. CCMP2 provides zonal and meridional components of winds 10 meters above the sea surface, which are used to compute WSP (Atlas et al., 2011).

2.2 WAVEWATCH 3 Model Hindcast

To complement our satellite data analysis, we use a wave hindcast produced by IFRE-MER using the WAVE-height, WATer depth and Current Hindcasting III (WW3) wave model forced by Climate Forecast System Reanalysis (CFSR) winds. Simulations span the period from 1993 to 2015 and are output at 6 hourly temporal and 0.5° spatial resolution. For model setup and validation, we refer the reader to Rascle and Ardhuin (2013).

In the supplementary material, we show our core analyses repeated with WW3 SWH and CFSR WSP (Figures S8-S9).

2.3 Monthly Climatology: Annual and Semi-Annual Variability

The analysis in this study focuses on annual and semi-annual variability as well as the mean states of the wave and wind fields using monthly averaged SWH and WSP. In order to analyze the annual and semi-annual variability, at each grid point, we perform a weighted least-squares fit to the mean, annual, and semi-annual cycles of SWH and WSP monthly climatologies. Annual and semi-annual cycles are represented as a sum of a sine and cosine, and fitted coefficients are used to infer amplitude and phase. Since 5 coefficients were least-squares fitted, IFREMER SWH grid locations were considered only if climatological means were available for at least 5 months of the year. In addition, to reduce errors associated with sparse sampling, we required that there be at least one climatological monthly mean in each of the four seasons. For weights, we use the standard error of the monthly climatology mean SWH and WSP. The number of independent observations for each monthly climatology average was computed using the decorrelation time scale over each month of CCMP2 WSP and IFREMER SWH daily data. Decorrelation time scales are computed from integrals of the lagged covariance (e.g., Gille, 2005), as discussed in the supplementary material. As a metric to evaluate the least-squares fit, we use fraction of variance explained (FVE) (Draper & Smith, 1998), defined as:

$$\text{FVE} = 1 - \frac{\sum_{i=1}^{N} \left(\frac{y_i - f_i}{\delta y_i}\right)^2}{\sum_{i=1}^{N} \left(\frac{y_i - \mu}{\delta y_i}\right)^2}, \tag{1}$$

where y_i is the ith monthly climatology mean data point with standard error δy_i, μ is the mean derived from the weighted least-squares fit of the data, and f_i is the ith model value. Data and model are weighted in (1) for consistency with the weighted least-squares fit. Since the weights represent the standard error of the mean, uncertainties inferred from the least-squares fit (e.g. Press et al., 1992) can be interpreted as the standard error of the mean of each fitted coefficient. Statistical uncertainties of the amplitude are computed using error propagation and thus represent the standard error of the mean amplitude. Amplitudes smaller than twice the standard error were judged not to be statistically different from zero. At grid points where the amplitude is not statistically significant, the phase is considered not well defined. See Figure S2 for fractional uncertainty for SWH and WSP amplitude.

166   Maps of the mean and standard deviation of SWH and WSP daily data in December-

167   January-February (DJF) and in June-July-August (JJA) illustrate the seasonal evolu-

168   tion and variance of the data (Figure 1). Monthly SWH and WSP climatologies were

169   computed for candidate expansion fan regions identified by Winant et al. (1988) by spa-

170   tially averaging monthly climatologies and their variances within 4° by 4° regions. We

171   selected 4° by 4° regions with anomalously high WSP, small spatial WSP gradients, and

172   annual cycle phases corresponding to WSP maxima during the late spring, summer, or

173   early fall. To minimize the effects of land contamination and inaccurate tidal corrections

174   for satellite altimetry SWH data (Bouffard et al., 2008), 4° by 4° regions are at least 1°

175   of longitude and latitude away from the coast. Uncertainties for SWH and WSP monthly

176   climatologies were computed by dividing the standard deviation (σ) by $\sqrt{N_{\text{eff}}}$ where N_{eff}

177   is the number of degrees of freedom to obtain the standard error of the mean ($\sigma/\sqrt{N_{\text{eff}}}$).

178   We estimated N_{eff} by averaging monthly temporal decorrelation scales (n_d), represent-

179   ing the number of data points between statistically independent measurements, into monthly

180   climatological averages, dividing the number of observations N used to compute the monthly

181   climatological average by the decorrelation scale such that $N_{\text{eff}} = N/n_d$, and then spa-

182   tially averaging N_{eff} over the 4° by 4° region. This approach assumes that the spatial

183   variation does not contribute to the degrees of freedom.

184   Basin-scale SWH and WSP annual cycles were obtained for the Northern and South-

185   ern Hemispheres of the Pacific, Atlantic, and Indian Oceans through weighted least-squares

186   fits of the monthly climatologies (see Figure S4 for basin-scale mean climatologies and

187   annual cycle fits). In targeted study regions, we compare the regional SWH climatology

188   to the basin-scale SWH annual cycle. To do this, we assume that the phasing of the SWH

189   is determined on a basin-scale (largely by high-latitude storms) while the mean SWH

190   and amplitude of the annual cycle can vary geographically. Thus we project the observed

191   local SWH onto the basin-scale fitted annual cycle. Differences between the two quan-

192   tify the deviation of the regional climatology from the expected hemispheric-scale an-

193   nual cycle.

3 Results and Discussion

3.1 Annual and semi-annual cycles in wind speed and significant wave height

Phase maps show that generally SWH and WSP are in phase, with both reaching maxima in their annual cycles in winter in both hemispheres. An exception occurs in the northern Indian Ocean, which is sheltered from high-latitude Northern Hemisphere winter storms (Figure 2A,B). In many regions across the globe, including high-latitude oceans, the tropical Atlantic and Pacific, and the region north of New Zealand, the SWH and WSP annual cycles are roughly in phase, implying that maximum wave height coincides in time with maximum WSP. However, several regions stand out in Figure 2A,B as deviating from these general patterns, either because WSP or SWH do not peak in winter or because WSP and SWH are out of phase with each other.

The annual cycle amplitude of both SWH and WSP (Figure 2E,F) is larger in the high-latitude Northern Hemisphere than in the high-latitude Southern Hemisphere, implying more seasonal variability in wave height and winds in the Northern Hemisphere than in the Southern Hemisphere. However, mean SWH and WSP are consistently higher in the Southern Hemisphere (Figure 1A-D). For SWH, high-amplitude annual cycles also occur in the Arabian Sea and in zonal bands from $\sim 30°$–$45°$ in the Northern and Southern Hemispheres. In the tropical Pacific and Atlantic, the SWH amplitude drops to near zero, but the WSP annual amplitude does not approach zero in the same locations.

The semi-annual cycle phases for SWH and WSP (Figure 2C,D) have more spatial structure than the corresponding annual cycle phases. However, many grid points are judged not to be statistically significant (white pixels in Figure 2C,D). In regions with high-amplitude WSP and SWH semi-annual cycles, including the Arabian Sea, Bay of Bengal, South China, and Southern Caribbean, WSP and SWH are in phase, with phase values indicating maxima or minima occurring in April and October.

The SWH and WSP semi-annual cycle amplitudes are smaller in magnitude than the annual cycles (Figure 2G,H). For both WSP and SWH, the regions with the highest amplitude semi-annual cycles occur in the Arabian and Southern Caribbean Seas. The Bay of Bengal and the South China Sea have high amplitude only for WSP. The South Asian monsoon's semi-annual occurrence may play a role in strong semi-annual

cycles, as the Arabian Sea, the Bay of Bengal, and the South China Sea are all monsoon regions.

Global maps of FVE (Figure 3A,B) assess the percentage of the variance explained by the mean plus annual and semi-annual cycles for SWH and WSP respectively. Features in the FVE maps for SWH and WSP align with features in the SWH and WSP annual and semi-annual amplitude maps (Figure 2): the percent of variation explained by the least-squares fit is highest in regions with high amplitude and lowest in regions of near zero amplitude or considered not statistically significant, with an exception for WSP off the coast of New Guinea. In locations where the annual and semi-annual cycles do not explain all of the temporal variability, local wind effects may be intermittent or simply governed by processes that are distinct from the annual and semi-annual cycle.

3.2 Waves: Swell Phase Discontinuities

In the equatorial Pacific and Atlantic, SWH phasing shows a sharp discontinuity between the Northern Hemisphere (boreal winter maximum) and the Southern Hemisphere (austral winter maximum) (Figure 2A). This phase transition, which we will refer to as a "swell phase discontinuity" occurs in regions of low to moderate seasonal mean SWH (Figure 1A,C) and low standard deviation (Figure 1E,G). It identifies the transition between regions with swell originating primarily in the Northern Hemisphere and swell primarily from the Southern Hemisphere. The swell phase discontinuity coincides geographically with "swell fronts" defined based on mean wave direction (I. R. Young, 1999; Semedo et al., 2011; Jiang & Chen, 2013). I. R. Young (1999) found that the Pacific and Atlantic swell front geographic locations vary seasonally. Since we define the swell phase discontinuity using SWH annual cycle phase, it represents an annually averaged signal that is expected to align with the annually averaged position of the swell front.

The swell phase discontinuity is slightly south of the equator in the western Pacific, between 5°S and 10°S west of 170°W, and it shifts equatorward further east (Figure 2A). In the Atlantic, the swell phase discontinuity aligns closely with the equator in the western Atlantic and abruptly shifts north of the equator near the western coast of

255 Africa. Explanations for the geographic location of these boundaries are beyond the scope

256 of the study and will be left for future research.

257   Just south of the swell phase discontinuity in the equatorial Pacific, several abrupt

258 shifts in phase exist between 10°S and 20°S at approximately 180°E and 145°W. These

259 are located on the northward facing sides of islands and are consistent with island shad-

260 owing: waves from the Southern Ocean propagating northward encounter the topogra-

261 phy of Polynesian islands and are blocked from traveling any further north. As a result,

262 waves vary with the Southern Hemisphere seasonal cycle to the south of the islands, and

263 vary with the Northern Hemisphere seasonal cycle to the north of the island (see Fig-

264 ure S1 for an enlarged map of the SWH annual cycle phase in the Polynesian island re-

265 gion).

266 **3.3 Winds: Identifying Seasonal Wind Anomaly Regions**

267   The WSP annual-cycle phase, ϕ_{wsp}, allows us to identify atypical regions, where

268 local winds are out of phase with hemispheric scale winds, providing a quantitative ap-

269 proach to identify SWARs. We define a SWAR as a region with a statistically signifi-

270 cant WSP annual cycle amplitude, with a phase that differs by 2.5 or more months from

271 the expected WSP phase ϕ_{exp} set by hemispheric large-scale storm systems,

$$|\phi_{wsp} - \phi_{exp}| \geq 2.5 \text{ months.} \tag{2}$$

272 Assuming that ϕ_{exp} corresponds to a WSP annual cycle reaching a maximum during the

273 middle of winter, mid-January in the Northern Hemisphere and mid-July in the South-

274 ern Hemisphere, the criterion in (2) is fulfilled when the WSP maximum occurs roughly

275 from April through October (boreal late spring, summer and early fall) for the North-

276 ern Hemisphere and from October through April (austral late spring, summer, and early

277 fall) for the Southern Hemisphere. Candidate SWARs determined by (2) are highlighted

278 in Figure 4. (Figure S3 provides global maps of SWARs using alternate criteria.)

279   For this analysis, marginal seas and the equatorial regions across the Pacific and

280 Atlantic Oceans are not considered. SWARs largely agree with the potential expansion

281 fan regions identified by Winant et al. (1988) with the exception of the Arabian Sea. This

282 metric also identifies some regions that were not suggested by Winant et al. (1988), in-

283 cluding the Central North and South Atlantic, the Central West African coast off An-

284 gola, the Southern Mozambique Channel, the North Indian Ocean, the Northwest and

Table 1. Candidate SWARs, identified using Equation 2, with figure number of SWAR's regional climatology. Expansion Fan regions are identified by Winant et al. (1988).

Expansion Fan Regions	Coastal	Open Ocean
West Australian coast (7A)	Central West African coast (S7B)	Central North Atlantic (S6C)
Namibian coast (7G)	Southern Mozambique Channel (S7C)	Central South Atlantic (S7A)
Chilean coast (7C)	Northwest Australian coast	North Indian Ocean (S7E)
Southern Caribbean Sea (6C)	Eastern Australian coast (S7F)	Mid-latitude Southern Pacific (S7D)
Northwest African Coast (6E)	Hawaii (S6A)	
California Coast (6A)	Southern Mexican coast (S6B)	
	Eastern South American coast	

Eastern Australian coasts, Hawaii, the mid-latitude Southern Pacific, the Southern Mexican coast and multiple small coastal regions along the eastern South American coast. Table 1 categorizes candidate SWARs into three groups: expansion fan wind regions identified by Winant et al. (1988), coastal regions, and open ocean regions. In the Southern Hemisphere, SWARs are concentrated in a zonal band from 15°S–30°S. From 66°S to 66°N latitude, we found that SWARs constitute approximately 3.39% of the ocean's surface area. SWARs highlighted by this approach could be generated by a broad range of meteorological phenomena other than expansion fan wind events.

3.4 Wind and Wave Relationships

By comparing the timing of the annual cycle phases, ϕ_{swh} and ϕ_{wsp}, we explore the relationship between local winds and the regional wave field, as illustrated in Figure 5. In high latitudes, local winds are in phase with waves, consistent with storms generating waves. Near the swell phase discontinuity and in most SWAR regions, local winds and waves are out of phase. From 66°S to 66°N latitude, WSP and SWH phases differ by 0 to 1 months for 57.13% of the ocean's surface area, while phase differences range from ±4-6 months for 1.65% of the ocean's surface area.

Within SWARs, the relationship between WSP and SWH annual cycle phases shows the impact of local winds on the wave field. We find two types of relationships: (a) waves,

aligned with hemispheric scales waves but out of phase with local winds and (b) waves, not aligned with hemispheric scale waves but in-phase with local winds.

In most SWARs, ϕ_{swh} and ϕ_{wsp} differ by 2 to 6 months (Figure 5), so that mean WSP reaches a maximum when mean SWH is near its minimum. Villas Bôas et al. (2017) described such a phase relationship within the California Current SWAR, where the WSP maximum occurs during boreal spring or summer. Since annual cycles in SWH are usually attributed to swell, high winds that are out of sync with high waves suggest the possibility of strong locally forced wind waves that peak at a different time of year than the swell generated in the same hemisphere as the SWAR. SWARs thus have the potential to have SWH that deviates from the annual cycle typical of swell originating from high-latitude storms. However, observations reveal that the extent to which local winds influence the wave field depends on regional wave and wind characteristics. Three characteristics of primary importance include exposure to swell generated in the high-latitude Northern or Southern Hemisphere, swell's annual cycle amplitude, and the strength of local winds. Among all SWARs, there are regions that have no exposure to Northern or Southern Hemisphere swell, regions with exposure to swell from one hemisphere, and regions with exposure to both Northern and Southern Hemisphere swell. Different combinations of these three characteristics lead to local winds having varied impacts on the regional wave field. Deviations from the annual cycle could also be attributed to swell originating in the high latitudes of the opposite hemisphere such that contributions to SWH from opposing hemisphere swell is greater than locally generated wind-seas. Furthermore, compared with the Northern Hemisphere, the Southern Hemisphere's low SWH annual cycle amplitude (Figure 2E) provides relatively consistent swell, making regions with significant exposure to the Southern Hemisphere experience less measurable influence from local winds.

Exceptions to the out-of-phase behavior in SWARs occur in the Arabian Sea, the Eastern Australian Coast, the South Mexican Coast, and the Southern Caribbean, where ϕ_{wsp} and ϕ_{swh} have a 0 to 1 month phase difference. This in-phase relationship, along with ϕ_{swh} reaching a maximum outside the timing of the expected hemispheric SWH annual cycle (Figure 2A), suggests that the waves within these SWARs are primarily locally forced, with little impact from remotely-forced swell.

3.5 Regional Climatologies of SWARs

In order to examine how phasing differences in the SWH and WSP annual cycles influence wave fields within SWARs, monthly climatologies for SWH and WSP were computed in 4° by 4° grid boxes centered on a core portion of the SWAR. Here we focus on SWARs in the potential expansion fan regions identified by Winant et al. (1988). Regional climatologies for all other SWARs can be found in the supplementary material (see Figures S5–S7). Calculations use data from January 1st, 1993 to December 31st, 2015 and focus on the individual boxes outlined in Figure 1B,D with enlarged maps in the left panels of Figures 6 and 7. The right panels of Figures 6 and 7 show SWAR regional climatologies for WSP (solid red) and SWH (solid blue) for the Northern and Southern Hemispheres, with the hemispheric SWH mean annual cycle computed as an average for the ocean basin (blue dashed line) and the residual between SWH climatology and basin-scale annual cycle (black, with gray shading). In Figures 6 and 7, WSP and SWH climatologies show distinctly different patterns depending on region. On the basin-scale, with the exception of the Indian Ocean (which we will address separately), SWH and WSP exhibit nearly the same basin-scale annual cycles in each ocean basin (Figure S4). This means that regional deviations in SWH cannot be attributed to geographic variations in basin-scale wind climatologies.

For Northern Hemisphere SWARs in eastern boundary current regions (i.e. the California Current in Figure 6A-B and North Africa in Figure 6E-F), the sharp summer peak in the WSP climatology (red) coincides with an anomalous augmentation in SWH (blue) relative to the basin-scale annual cycle (blue dashed line). In both cases, the observed augmentations deviate by more than twice the standard error from the basin-scale annual cycle.

In contrast, in the Southern Hemisphere eastern boundary current areas, with the exception of western Australia (i.e. the Chilean coast in Figure 7D-E and the Namibian coast in Figure 7F-G), we see broad summer increases in WSP extending from October or November through February or March (red) that correspond to small magnitude deviations of SWH (blue) of less than 0.5 standard errors from the basin-scale annual cycle. These results imply that in Southern Hemisphere SWARs (Figure 7), local winds have comparatively less influence on the wave climate than in the Northern Hemisphere, possibly because strong year-round winds in the high-latitude Southern Hemi-

–13–

sphere lead to a smaller seasonal cycle in Southern Hemisphere swell (Figure 2A) and more overall wave energy than in the Northern Hemisphere. Against this background level of wind and swell, locally-induced anomalies in the Southern Hemisphere are expected to be less distinct than in the Northern Hemisphere. The Indian Ocean is unusual in displaying a basin-scale WSP maximum in the austral summer months in addition to an austral winter maximum, which complicates interpretation of processes governing SWAR WSP and SWH. Off the coast of Western Australia (Figure 7A-B), the summer WSP peak that extends from December to February is particularly strong and corresponds to a 0.38 m SWH deviation (more than 3 standard errors) from the Indian Ocean's annual cycle. This is near the same magnitude as deviations in the Northern Hemisphere, suggesting that Western Australia's local winds are strong enough to influence the wave field at a level similar to Northern Hemisphere SWARs. The basin-scale WSP local maximum during austral summer may also play a role in determining the magnitude of the deviation.

The monsoon region in the Arabian Sea (Figure 7G-H) and the tropical storm region in the southern Caribbean Sea (Figure 6C-D) have distinctly different wind and wave climatologies than the eastern boundary current regions. Both regions are characterized by strong semi-annual cycles in WSP (red lines in Figures 6D and 7H), and by SWH that varies with the semi-annual WSP (blue lines in Figures 6D and 7H). In the Caribbean, SWH shows almost no annual cycle (blue dotted line in Figure 6D), and in the Arabian Sea the annual cycle in SWH captures only a portion of the overall SWH variability. In both regions, the significance of the SWH semi-annual cycle compared with the annual cycle is demonstrated by the large deviations from the annual cycle (gray shading in Figures 6D and 7H). These patterns imply that semi-annually varying local winds are important drivers of SWH in these regions. The Antilles archipelago shelters the Southern Caribbean SWAR from waves propagating from high latitudes (Semedo et al., 2011) (Figure 6C). The lack of annual cycle in the SWH is consistent with the hypothesis that Caribbean SWH is forced entirely by local winds. In contrast, the Arabian Sea is not fully sheltered from remotely generated swell, and Indian Ocean WSP has a distinct pattern of semi-annual variability, meaning that SWH in the Arabian Sea could result from a combination of locally forced wind waves and remotely forced swell.

3.6 Wind-sea vs. Swell Dominance in SWARs

The phase differences and climatologies discussed in the preceding sections suggest the likely distinctions between remotely forced swell and locally forced wind waves. Phase differences between local SWH and hemispheric wind and wave climatologies can also occur if a region has significant exposure to swell propagating from the opposite hemisphere.

One method to distinguish swell from wind-sea is through wave age, which quantifies the stage of development of waves (Alves et al., 2003). Here we use the wave age criterion of Donelan et al. (1992), defined as:

$$\text{Wave Age} = \frac{C_p}{U_{10}}, \tag{3}$$

where C_p is the phase speed at the peak frequency of the wave spectrum, and U_{10} is the wind speed at 10 m elevation. For $C_p/U_{10} \leq 1.2$, the wave field is considered to be dominated by wind-sea and highly coupled to the local winds, with wind still supplying momentum to waves. For $C_p/U_{10} > 1.2$, the wave field is considered to be dominated by swell, where waves travelling 20% faster than U_{10} are outrunning the wind and not receiving momentum from the wind. For deep water waves, which are the focus of this paper, with peak frequency f_p, the dispersion relationship yields the peak phase speed:

$$C_p = \frac{g}{2\pi f_p}. \tag{4}$$

The wave field can be composed of a superposition of multiple wave systems. The peak phase speed represents the phase speed of the most energetic wave system. Thus, although both swell and wind-sea are likely to co-exist in the wave field, the separation process categorizes the wave field as being dominated either by swell or by wind-sea waves.

Using wave age, probability of swell can be obtained to estimate the fraction of time that the wave field is swell-dominated relative to the total number of wave measurements:

$$\text{Probability of swell} = \frac{N_{swell}}{N_{total}}, \tag{5}$$

where N_{swell} is the number of observations with wave age exceeding 1.2 representing a swell-dominated wave field and N_{total} is the total number of observations in the time series. Probability of swell provides a metric to evaluate whether the atypical wind climatology within a SWAR is responsible for wind-seas during the late spring, summer, and early fall.

424   Previous global estimates of probability of swell (Semedo et al., 2011; Jiang & Chen,

425 2013; Zheng et al., 2016) have shown that remotely forced waves dominate the wave field

426 in all ocean basins with the exception the Southern Ocean, some coastal regions, and com-

427 mon storm tracks, where wind-generated waves play a stronger role. Here, we comple-

428 ment their results by focusing on regional analysis of SWARs. For probability of swell

429 calculations we use WW3 SWH. Figures S8-S9 in the supplementary material show that

430 WW3 SWH annual cycles resemble IFREMER SWH annual cycles.

431   The seasonal progression of probability of swell computed using C_p and U_{10} from

432 the WW3 hindcast (Figure 8) is consistent with the findings of Semedo et al. (2011). First

433 we consider the expansion fan SWARs identified by Winant et al. (1988). In these re-

434 gions, the wave field is dominated by wind-seas a higher percentage of time than it is in

435 surrounding regions. Wind-seas occur most typically during the late spring and early sum-

436 mer months (Figure 8A,C). For the Northern Hemisphere, off the coasts of California

437 and North Africa, the probability of swell drops to 80%–90% in spring and 60%–70% in

438 summer. The Caribbean Sea has probabilities of swell below 75% through the entire year,

439 with typical values ranging from 20%–40%, suggesting that the wave field consistently

440 experiences stronger influence from local winds than most regions. In the Southern Hemi-

441 sphere, the probability of swell in the SWARs of West Australia, Chile, and Namibia ranges

442 from 90% to 95%, which is not as low as in Northern Hemisphere SWARs. In the Ara-

443 bian Sea, probability of swell drops to 60%–70% in the summer. These results are con-

444 sistent with the hypothesis that the deviation from the basin-scale SWH annual cycle

445 in SWARs results from locally forced wave contributions to SWH. The results also sup-

446 port the hypothesis that compared with the Northern Hemisphere SWARs, Southern Hemi-

447 sphere SWARs are less likely to be dominated by locally forced waves because of their

448 close proximity to persistent swell originating from the Southern Ocean.

449   One region of interest is the small coastal SWAR off the southern coast of Brazil

450 near Rio de Janeiro (Figure 4A,D), where the probability of swell drops below 75% dur-

451 ing austral spring and summer. Although this SWAR was not identified by Winant et

452 al. (1988), its low probability of swell during austral summer and its coastal location sug-

453 gest that the region has characteristic traits of expansion fan wind regions and may in

454 fact experience expansion fan winds despite being on a western boundary.

The second and three columns in Table 1 identify SWARs not identified as expansion fan regions by Winant et al. (1988) (see Figure 4). In these areas, the wave field is dominated by swell a high percentage of the time during the late spring, summer and early fall. With the exception of the Mexican coast, the probability of swell is 95%–100% in these SWARs. Off the Mexican coast, the probability of swell drops to 85%–90% in the boreal fall. This indicates that open-ocean and some coastal SWARs have regional wave and wind characteristics that are unfavorable for wind seas.

4 Conclusion

In this paper, we have explored waves and winds separately, examining the seasonal cycle of WSP and SWH and closely examining regions where the seasonal cycles of winds and waves deviate from the seasonal cycle typically seen in the surrounding ocean basins. Atypical wave seasonal cycles are found within the equatorial region, where we see a sharp SWH phase transition, referred to as a swell phase discontinuity. Atypical WSP seasonal cycles, out of phase with hemispheric-scale winds, are identified as SWARs and are located in eastern boundary current regions, monsoon regions, and regions significantly sheltered from remotely forced waves. In total, 3.39% of the world oceans from 66°S to 66°N latitude experience anomalous WSP seasonal variability.

The wave response to local winds is investigated to determine whether the characteristic features of the wind and wave fields observed off the California coast by Villas Bôas et al. (2017) are present in other SWARs. We find that most SWARs exhibit a 2–6 month phase difference between WSP and SWH annual cycles. However, anomalous patterns of wind variability do not necessarily drive anomalous patterns of wave climatology. Within potential expansion fan SWARs identified by Winant et al. (1988), SWH deviates from the SWH seasonal cycle in the Northern Hemisphere but shows a low-to-zero magnitude deviation in the Southern Hemisphere. Exceptions to these phasing patterns occur along the southern Mexican coast, in the South Caribbean, in monsoon regions, and on the Eastern Australian coast, where local winds dominate over hemispheric-scale seasonal wind patterns. In these regions, the wave climate is consistent with a response to local winds. While there are commonalities between SWARs, the fraction of wave variability attributed to local wind events varies depending on regional and wave field characteristics, suggesting that the statistics that define the coastal California SWAR are not universal, and each SWAR varies in slightly different ways depending on local conditions.

487   Probability of swell is used as a diagnostic to distinguish locally forced waves from

488 remotely-forced swell. Within SWARs associated with expansion fan winds, during spring

489 and summer months, probability of swell is lower than in surrounding regions, imply-

490 ing wind-seas and SWH due to locally forced winds. This supports the hypothesis that

491 the deviation from the SWH annual cycle results from waves that are forced by local wind

492 events.

493   We have presented a method to evaluate the relative importance of wind-sea and

494 swell from mean behavior of the wave field without the need for directional wave spec-

495 tra. Improved understanding of the SWH response to local wind events has the poten-

496 tial to lead to more accurate model representations of the wave climate in SWARs. In

497 the future, global observations of directional wave spectra from remote sensing platforms

498 such as the Chinese-French Oceanography Satellite CFOSAT and other proposed Doppler

499 oceanography mission concepts have the potential to further our understanding of the

500 effects of local winds on the wave climate: the addition of direction and frequency in-

501 formation would help to distinguish the roles of swell, wind-seas, and mixed seas in de-

502 termining wave conditions under different wind regimes across the globe and to better

503 quantify the contribution of local winds to regional wave climates.

Data Availability Statement

510   The data necessary to reproduce all results from this paper is currently available

511 through Google Drive for the purposes of peer review `https://drive.google.com/drive/`

512 `folders/1fxhS00Oz8CSbYIUxcDfann2s65t3m5-B?usp=sharing`, and it will be any pub-

513 licly available through the University of California, San Diego library digital collections

514 `https://library.ucsd.edu/dc/` (doi will be provided upon acceptance). The source

515 code used to produce the figures can be accessed on GitHub: `https://github.com/lcolosi/`

516 `WaveClimatology`.

517   If the reader is interested in accessing the raw data, they may visit `http://www.remss`

518   `.com/measurements/ccmp/` for the CCMP Version-2.0 vector wind analysis product, `ftp://`

519   `ftp.ifremer.fr/ifremer/cersat/products/swath/altimeters/waves` for the satel-

520   lite altimetry significant wave height product, and `ftp://ftp.ifremer.fr/ifremer/`

521   `ww3/HINDCAST` for the WAVEWATCH 3 hindcast significant wave height, surface wind

522   velocity, and peak wave frequency.

References

524   Alves, J. H. G., Banner, M. L., & Young, I. R.   (2003).   Revisiting the Pierson–

525   Moskowitz asymptotic limits for fully developed wind waves.   *Journal of Phys-*

526   *ical Oceanography*, *33*(7), 1301–1323.   doi: 10.1175/1520-0485(2003)033⟨1301:

527   RTPALF⟩2.0.CO;2

528   Ardhuin, F. (2020). *Ocean waves in geosciences.* doi: 10.13140/RG.2.2.16019.78888/

529   5

530   Ardhuin, F., Stopa, J. E., Chapron, B., Collard, F., Jensen, R. E., Johannessen, J.,

531   . . . others (2019). Observing sea states. *Frontiers in Marine Science*, *6*, 124.

532   doi: 10.3389/fmars.2019.00124

533   Atlas, R., Hoffman, R. N., Ardizzone, J., Leidner, S. M., Jusem, J. C., Smith,

534   D. K., & Gombos, D.   (2011).   A cross-calibrated, multiplatform ocean sur-

535   face wind velocity product for meteorological and oceanographic applica-

536   tions.   *Bulletin of the American Meteorological Society*, *92*, 157-174.   doi:

537   10.1175/2010BAMS2946.1

538   Bouffard, J., Vignudelli, S., Cipollini, P., & Menard, Y.   (2008).   Exploiting the po-

539   tential of an improved multimission altimetric data set over the coastal ocean.

540   *Geophysical Research Letters*, *35*(10). doi: 10.1029/2008GL033488

541   Cavaleri, L., Fox-Kemper, B., & Hemer, M.   (2012).   Wind waves in the coupled cli-

542   mate system.   *Bulletin of the American Meteorological Society*, *93*(11), 1651–

543   1661. doi: 10.1175/BAMS-D-11-00170.1

544   Donelan, M., Skafel, M., Graber, H., Liu, P., Schwab, D., & Venkatesh, S.   (1992).

545   On the growth rate of wind-generated waves.   *Atmosphere-Ocean*, *30*(3), 457–

546   478. doi: 10.1080/07055900.1992.9649449

547   Draper, N. R., & Smith, H. (1998). *Applied regression analysis* (Vol. 326). John Wi-

548   ley & Sons. doi: 10.1002/9781118625590

Echevarria, E., Hemer, M., & Holbrook, N. (2019). Seasonal variability of the global spectral wind wave climate. *Journal of Geophysical Research: Oceans*, *124*(4), 2924–2939. doi: 10.1029/2018JC014620

Edson, J., Crawford, T., Crescenti, J., Farrar, T., Frew, N., Gerbi, G., ... others (2007). The coupled boundary layers and air–sea transfer experiment in low winds. *Bulletin of the American Meteorological Society*, *88*(3), 341–356. doi: 10.1175/BAMS-88-3-341

Gille, S. T. (2005). Statistical characterization of zonal and meridional ocean wind stress. *Journal of Atmospheric and Oceanic Technology*, *22*(9), 1353–1372. doi: 10.1175/JTECH1789.1

Jiang, H., & Chen, G. (2013). A global view on the swell and wind sea climate by the Jason-1 mission: A revisit. *Journal of Atmospheric and Oceanic Technology*, *30*(8), 1833–1841. doi: 10.1175/JTECH-D-12-00180.1

Munk, W. H. (1951). *Origin and generation of waves* (Tech. Rep.). La Jolla, CA, USA: Scripps Institution of Oceanography.

Press, W. H., Teukolsky, S. A., Flannery, B. P., & Vetterling, W. T. (1992). *Numerical recipes in fortran 77: volume 1, volume 1 of fortran numerical recipes: the art of scientific computing.* Cambridge university press.

Queffeulou, P. (2004). Long–term validation of wave height measurements from altimeters. *Marine Geodesy*, *27*(3-4), 495–510. doi: 10.1080/01490410490883478

Queffeulou, P., & Croizé-Fillon, D. (2017). *Global altimeter SWH data set* (Vol. 2; Tech. Rep.). ZI de la Pointe du Diable, CS10070, 29280 Plouzané, France: IFREMER.

Rascle, N., & Ardhuin, F. (2013). A global wave parameter database for geophysical applications. Part 2: Model validation with improved source term parameterization. *Ocean Modelling*, *70*, 174–188. doi: 10.1016/j.ocemod.2012.12.001

Semedo, A. (2018, Mar). Seasonal variability of wind sea and swell waves climate along the canary current: The local wind effect. *Journal of Marine Science and Engineering*, *6*(1), 28. doi: 10.3390/jmse6010028

Semedo, A., Sušelj, K., Rutgersson, A., & Sterl, A. (2011). A global view on the wind sea and swell climate and variability from ERA-40. *Journal of Climate*, *24*(5), 1461–1479. doi: 10.1175/2010JCLI3718.1

582 Snodgrass, F. E., Hasselmann, K. F., Miller, G. R., Munk, W. H., & Powers, W. H.
583   (1966).   Propagation of ocean swell across the Pacific.   *Philosophical Trans-*
584   *actions of the Royal Society of London. Series A, Mathematical and Physical*
585   *Sciences*, *259*(1103), 431–497. doi: 10.1098/rsta.1966.0022

586 Stopa, J. E.   (2019).   Seasonality of wind speeds and wave heights from 30 years of
587   satellite altimetry.   *Advances in Space Research*.   doi: 10.1016/j.asr.2019.09
588   .057

589 Stopa, J. E., & Cheung, K. F.   (2014).   Periodicity and patterns of ocean wind and
590   wave climate.   *Journal of Geophysical Research: Oceans*, *119*(8), 5563–5584.
591   doi: 10.1002/2013JC009729

592 Sullivan, P. P., McWilliams, J. C., & Melville, W. K.   (2004).   The oceanic bound-
593   ary layer driven by wave breaking with stochastic variability. Part 1. Direct
594   numerical simulations.   *Journal of Fluid Mechanics*, *507*, 143–174.   doi:
595   10.1017/S0022112004008882

596 Sverdrup, H. U., & Munk, W. H.   (1947).   *Wind, sea and swell: Theory of relations*
597   *for forecasting* (No. 303). Hydrographic Office. doi: 10.5962/bhl.title.38751

598 Villas Bôas, A. B., Ardhuin, F., Ayet, A., Bourassa, M. A., Brandt, P., Chapron,
599   B., . . . others   (2019).   Integrated observations of global surface winds, cur-
600   rents, and waves: requirements and challenges for the next decade. *Frontiers in*
601   *Marine Science*, *6*. doi: 10.3389/fmars.2019.00425

602 Villas Bôas, A. B., Gille, S. T., Mazloff, M. R., & Cornuelle, B. D.   (2017).   Charac-
603   terization of the deep water surface wave variability in the California Current
604   region.   *Journal of Geophysical Research: Oceans*, *122*(11), 8753–8769.   doi:
605   10.1002/2017JC013280

606 Winant, C. D., Dorman, C. E., Friehe, C. A., & Beardsley, R. C. (1988). The marine
607   layer off northern California: An example of supercritical channel flow. *Journal*
608   *of the Atmospheric Sciences*, *45*(23), 3588–3605. doi: 10.1175/1520-0469(1988)
609   045⟨3588:TMLONC⟩2.0.CO;2

610 Young, I., Zieger, S., & Babanin, A. V.   (2011).   Global trends in wind speed and
611   wave height. *Science*, *332*(6028), 451–455. doi: 10.1126/science.1197219

612 Young, I. R. (1999). Seasonal variability of the global ocean wind and wave climate.
613   *International Journal of Climatology: A Journal of the Royal Meteorologi-*
614   *cal Society*, *19*(9), 931–950.   doi: 10.1002/(SICI)1097-0088(199907)19:9⟨931::

615   AID-JOC412⟩3.0.CO;2-O

616   Young, I. R., Fontaine, E., Liu, Q., & Babanin, A. V. (2020). The wave climate of

617   the Southern Ocean. *Journal of Physical Oceanography*, *50*(5), 1417–1433. doi:

618   10.1175/JPO-D-20-0031.1

619   Zheng, K., Sun, J., Guan, C., & Shao, W. (2016). Analysis of the global swell and

620   wind sea energy distribution using WAVEWATCH III. *Advances in Meteorol-*
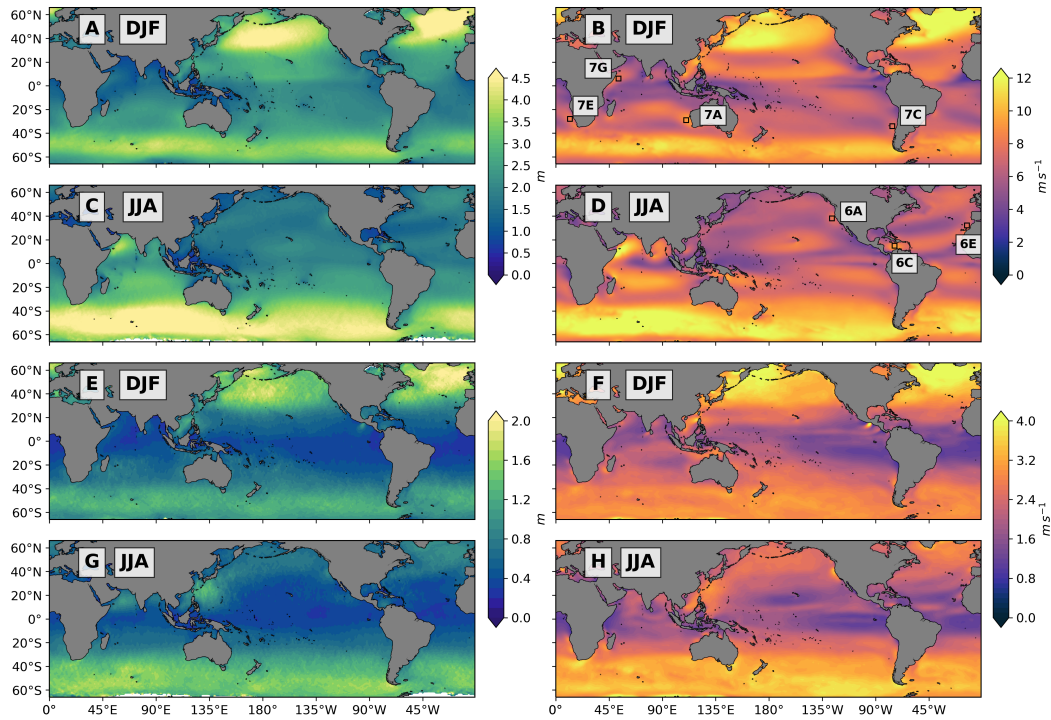
621   *ogy*, *2016*. doi: 10.1155/2016/8419580

Figure 1. DJF seasonal mean for (A) IFREMER SWH and (B) CCMP2 WSP; JJA seasonal mean for (C) IFREMER SWH and (D) CCMP2 WSP; DJF standard deviation of daily data for (E) IFREMER SWH and (F) CCMP2 WSP; JJA standard deviation of daily data for (G) IFREMER SWH and (H) CCMP2 WSP. See text for details of computation. Black boxes in (B) and (D) indicate the selected regions for monthly climatology analysis in the Southern and Northern Hemispheres, respectively.
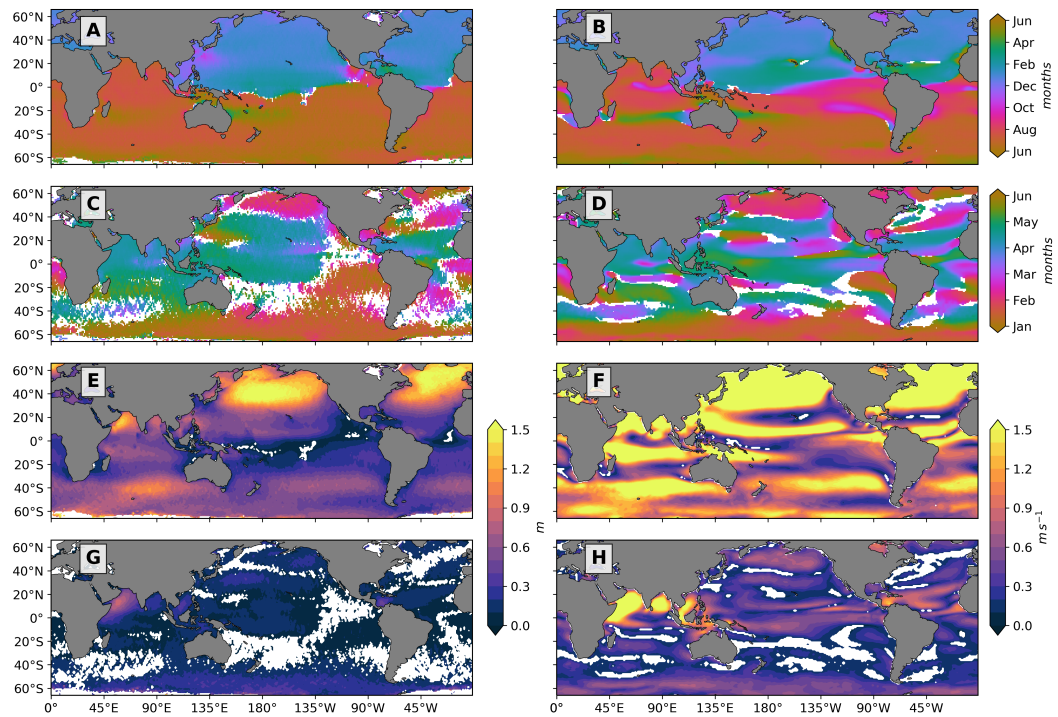
Figure 2. Phase of annual cycle for (A) IFREMER SWH and (B) CCMP2 WSP; phase of semi-annual cycle for (C) IFREMER SWH and (D) CCMP2 WSP; amplitude of annual cycle for (E) IFREMER SWH and (F) CCMP2 WSP; amplitude of semi-annual cycle for (G) IFREMER SWH and (H) CCMP2 WSP. Amplitudes less than or equal to twice the standard error are not considered statistically significant and masked white; the same pixels are also masked for phase. See section 2.3 for details of computation. Phase is indicated in months. Streak patterns in A, C, E, and G are an artifact of the altimeter sampling patterns and should not be interpreted as robust signal. (Comparison plots showing equivalent quantities for WW3 and IFREMER SWH and CFSR and CCMP2 WSP can be found in Figure S8 of the supplementary material).
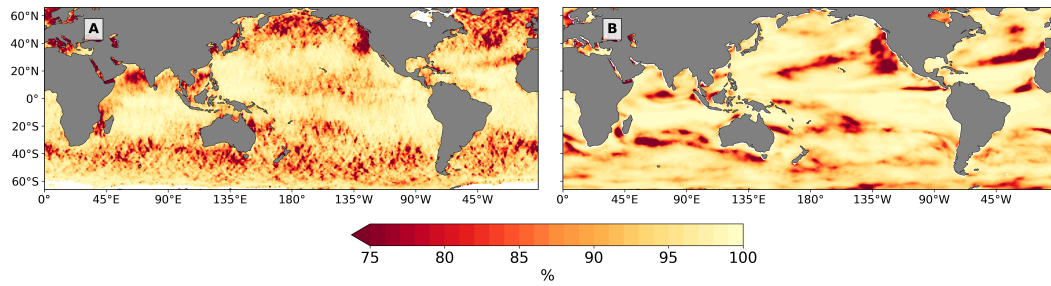
Figure 3. Fraction of variance explained by weighted annual and semi-annual least squares fit for IFREMER SWH (A) and CCMP2 WSP (B) from January 1st, 1993 to December 31st, 2015.
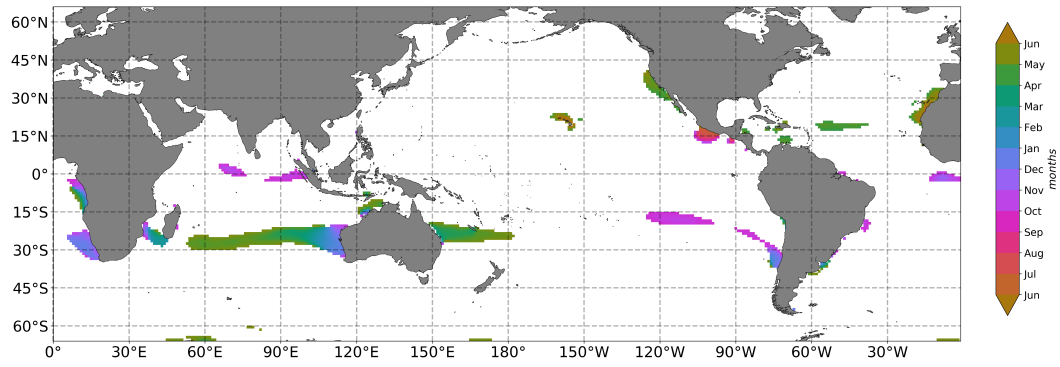
Figure 4. Annual cycle phase for CCMP2 wind speed, highlighting SWARs using the WSP maximum criteria. White pixels correspond to points that are not categorized as having anomalous phase or where the amplitude is not statistically significant.
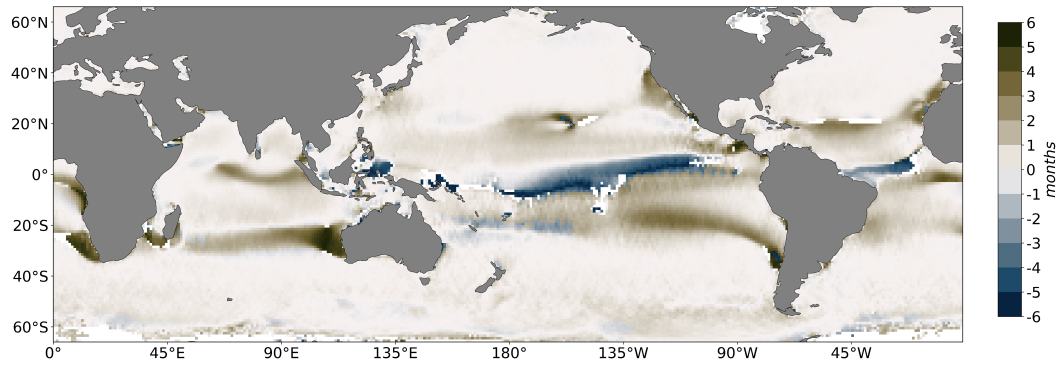
Figure 5. Difference between the annual cycle phases, ϕ_{wsp} and ϕ_{swh}. White pixels correspond to points where phase differences are not statistically significant, or where the annual cycle amplitude is small enough that phase is not well defined.
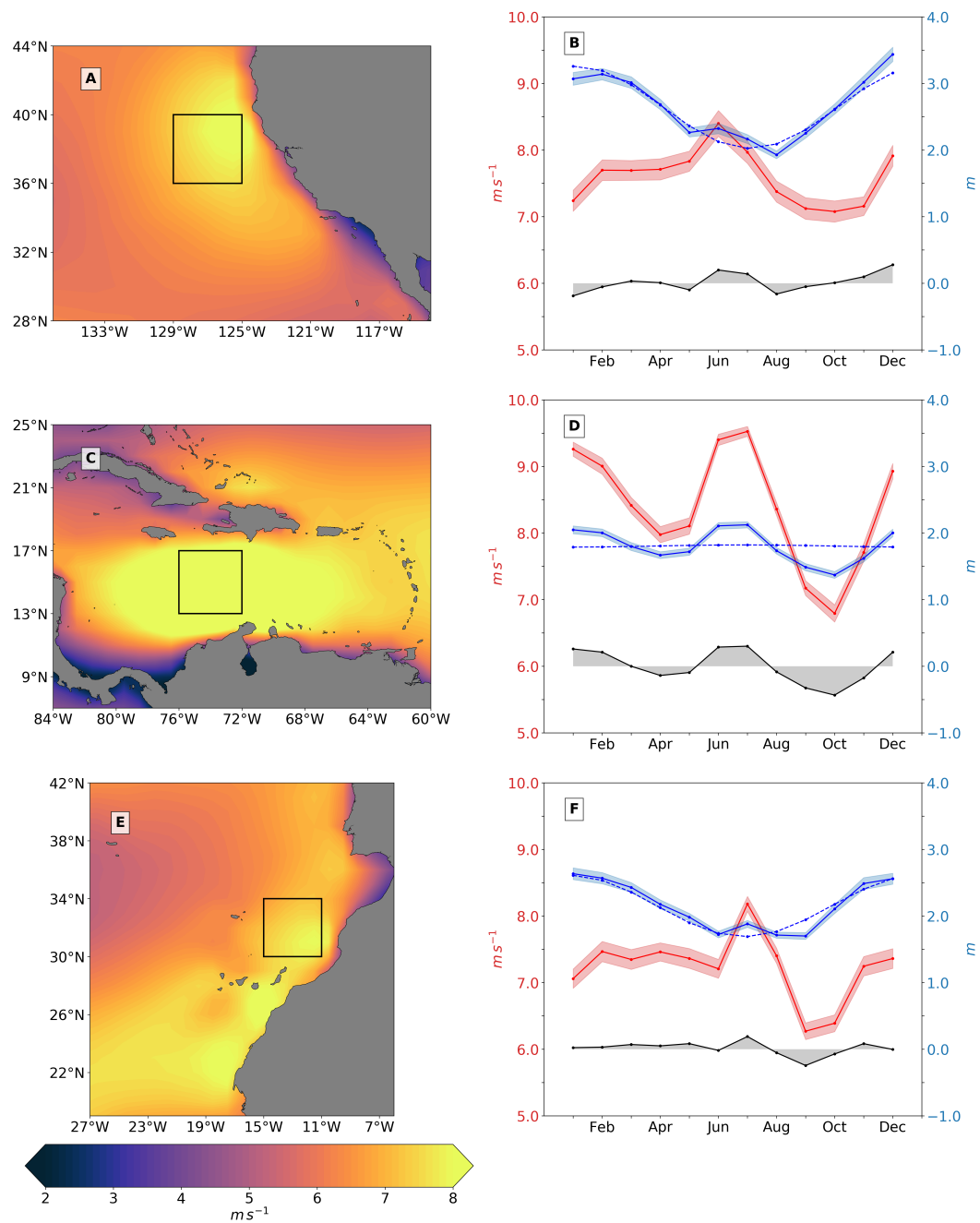
Figure 6. (left column) Northern Hemisphere wind speed in SWARs, averaged over June, July, and August. (right column) IFREMER SWH (solid blue) and CCMP2 WSP (solid red) climatologies extracted from the outlined 4° by 4° boxes within SWARs. Blue shading represents the standard error of the mean, dotted blue is the annual cycle weighted least-squares fitted to monthly climatology for mean SWH of the hemisphere ocean basin the SWAR is located in, and black solid is the residual between SWH regional climatology and annual cycle. SWARs include Northern California (A and B), Southern Caribbean Sea (C and D), and North Africa near the coast of Morocco and western Sahara (E and F). (Comparison plots showing equivalent quantities for WW3 and IFREMER SWH and CFSR and CCMP2 WSP can be found in Figure S9A,C,E of the supplementary material).
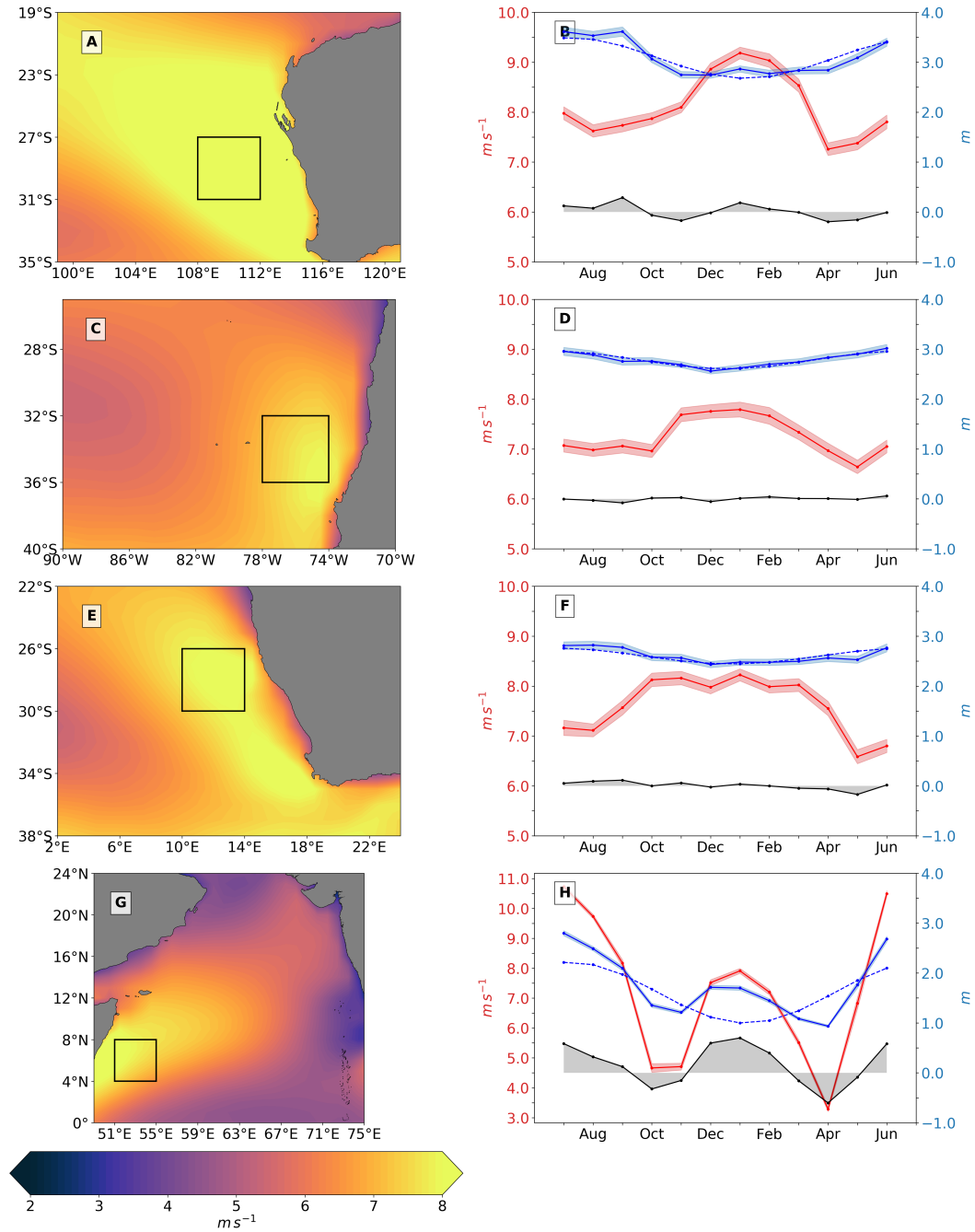
Figure 7. (left column) Southern Hemisphere wind speed in SWARs, averaged December, January, and February with (right column) IFREMER SWH (solid blue) and CCMP2 WSP (solid red) climatologies from the shaded 4° by 4° boxes. Shading, dotted lines, and solid black are as in Figure 6. SWARs include Western Australia (A and B), Central Western coast of South America near Chile (C and D), South-Western Coast of Africa near Namibia (E and F), and North-Western Arabian Sea (G and H). (Comparison plots showing equivalent quantities for WW3 and IFREMER SWH and CFSR and CCMP2 WSP can be found in Figure S9B,D,F,G of the supplementary material).
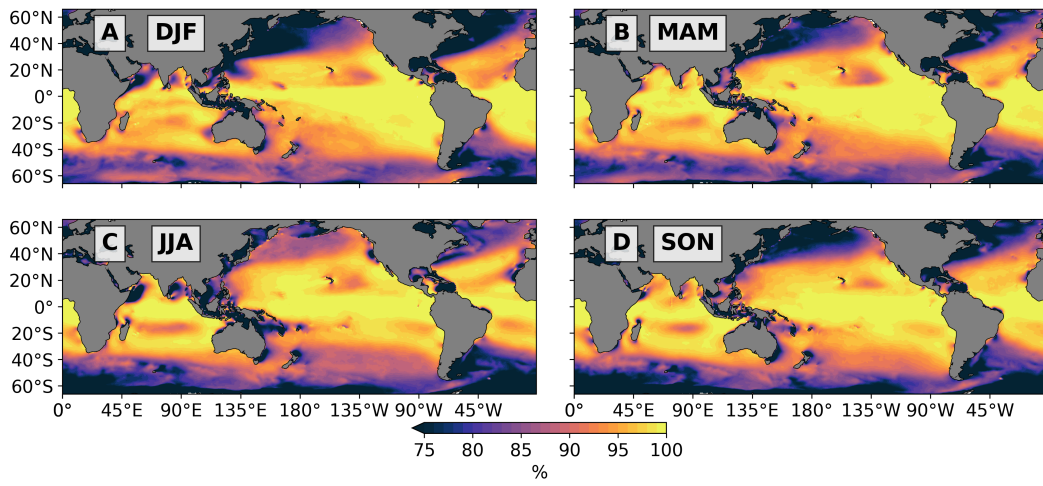
Figure 8. Seasonal progression of probability of swell using wave age criterion (3) and WW3 peak frequency and WSP from January 1st, 1993 to December 31st, 2015 where (A) DJF, (B) MAM, (C) JJA, and (D) SON

.